A density functional theory study of CrSBr for spin-orbit-torque magnetic random-access memory

by

Carter Rodny

B.S., University of Colorado - Boulder, 2022

A REPORT

submitted in partial fulfillment of the requirements for the degree

MASTER OF SCIENCE

Department of Chemical Engineering
Carl R. Ice College of Engineering

KANSAS STATE UNIVERSITY
Manhattan, Kansas

2026

Approved by:

Major Professor
Bin Liu, PhD

Copyright

Abstract

The explosive growth of artificial intelligence and data center infrastructure is driving a surge in global electricity demand. Projections indicate that data centers could consume 12% of U.S. electricity by 2028, and global electricity consumption could double by 2030 (Lawson, 2026). Conventional, charge-based memory architectures suffer from the von Neumann bottleneck and high leakage power, motivating the development of spintronic alternatives (Chen, 2023). Among spintronic memory technologies, the spin-orbit-torque magnetic random-access memory (SOT-MRAM) stands out for its speed, endurance, and read-write separation (Song, 2023). To make this technology practical at scale, it must overcome its current external-field requirements for deterministic switching.

This work investigates CrSBr, an air-stable van der Waals antiferromagnet (AFM), as a symmetry-breaking layer for exchange-bias SOT ferromagnets (FM) (Ziebel, 2024). Using DFT calculations, this study examines FM, AFM, and hydrogen-doped CrSBr variants. Geometry optimizations yield lattice parameters in excellent agreement with experiment (Ziebel, 2024). The calculated magnetic moments confirm the expected A-type AFM ordering, and reveal that while the hydrogen dopant largely preserves the interlayer AFM, it introduces a small net moment that drives a semiconductor-to-metal transition. Band structures and density-of-states show spin splitting in the FM phase and degeneracy in the AFM phase. These results show the destructive effect hydrogen contamination may have on these systems, as well as potential opportunities for bandgap engineering through light doping.

Table of Contents

List of Figures

List of Tables

Acknowledgements

I would like to thank Dr. Bin Liu for the time and effort he has poured into me throughout my experience at Kansas State University. His passion for computational methods has been inspiring to my own work and pushed me to dive deeper into my research. It was always encouraging to see the passion he has for his students and for raising the next generation of engineers. I would also like to thank my supervisory committee members, Dr. Placidus Amama and Dr. James Edgar, for their teaching and support during my academic experience.

Introduction

The rate of digitalization is accelerating at an unprecedented pace. The adoption of large language models (LLMs), advanced AI platforms, and the ever-growing construction of data centers are demanding a significant amount of power from an already strained system. The U.S. Congress reported that in 2023, data centers accounted for 4.4% of US energy consumption (Lawson, 2026). With exponentially increasing demand for AI, models predict this could reach 12% of total US energy consumption by 2028 (Lawson, 2026). The IEA predicts global data center energy consumption will nearly double over the next four years. The estimates for each region are shown in Figure 1.

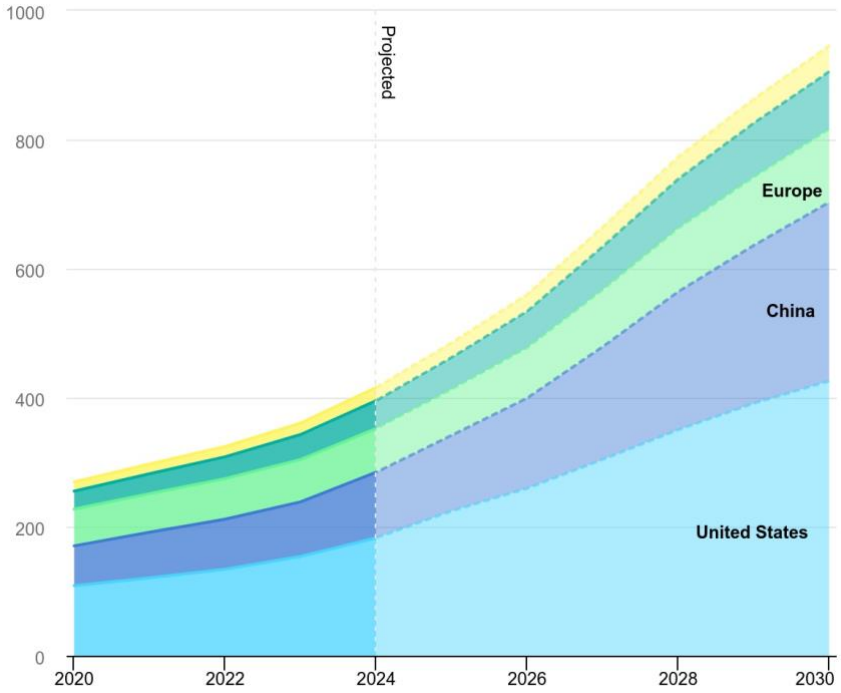

Figure 1: Data center electricity consumption (TWh) by region, 2020-2030.

License: CC BY 4.0. International Energy Agency. (2025). Data center electricity consumption by region, Base Case, 2020-2030 [Chart]. https://www.iea.org/data-and-statistics/charts/data-centre-electricity-consumption-by-region-base-case-2020-2030

As the data industry grows, more efficient technologies must be developed to slow the intensifying demand for power. One major cause of energy inefficiency is that conventional computer architecture relies on inefficient transfers between the CPU and memory units, commonly referred to as the von Neumann bottleneck (Chen, 2023), which slows computational speed and increases energy consumption via Joule heating (Chen, 2023). Spintronic systems offer a solution to this problem by processing and storing data in a single local area (Chen, 2023).

Conventional RAM also relies on charged or uncharged capacitors to store bits. This requires a continuous recharging of the capacitors to maintain information integrity. Spintronics solutions have been shown to have zero leakage power dissipation and significant sleep energy power savings (Huang, 2014).

Spintronic solutions offer highly tunable alternatives to traditional electronics by harnessing electron spins, in addition to their charge. The benefits of spintronic systems include memory retention even when powered off, low-power consumption, and scalability (Chen, 2023). Spintronics have gained significant traction in the past decade as innovations have made them increasingly relevant to AI and quantum computing applications.

The field of spintronics began in the late 80s with the discovery of the giant magnetoresistor (GMR) (Baibich, 1988). Both French physicist Albert Fert and German physicist Peter Grünberg independently designed and built their GMR devices, later earning them the 2007 Nobel Prize in Physics (Ornes, 2013). Their GMR devices consisted of thin, alternating layers of iron and chromium (Baibich, 1988; Binasch, 1989). Initially, the iron layers were AFM. Upon application of an external magnetic field, the iron layers flipped to FM

alignment, and the resistance of the superlattice decreased by up to 50% (Binasch, 1989). They attributed this observation to spin-dependent scattering, and thus spintronics was born.

A decade later, advances in sputtering technologies have allowed the development of these devices on an industrial scale. GMR layering via sputtering techniques was achieved on magnetic read heads, enabling the reading of hard disk drives (Nobel Prize Outreach, 2007). This was the first commercial spintronic product and set the stage for the industry for the next decade.

Researchers began to shift their focus to the use of spintronics principles in advanced memory and logic applications. A major milestone was achieved with the development of magnetic random-access memory (MRAM), which uses magnetic tunnel junctions (MTJs) rather than capacitors for bit storage (Gallagher, 2006). They relied on external magnetic fields to switch the magnetic state of the free layer (Gallagher, 2006). These devices enabled energy-efficient, non-volatile, high-speed RAM. Higher-efficiency developments emerged in the 2010s with the advent of spin-transfer torque magnetoresistance RAMs (STT-MRAMs). These devices run a current of spin-polarized electrons directly to the free layer to torque and flip its moment between states (Huang, 2014). This enables greater scalability, speed, density, and endurance (Huang, 2014).

Over the past five years, significant research has focused on optimizing these technologies for mass-production foundry processes and integration into systems to improve efficiency, reliability, and scaling. Material selection, optimization, and manufacturability are major drivers for these improvements. 2D van der Waals (vdW) materials are especially appealing as they offer magnetic tunability and stacking configurations (Ziebel, 2024). CrSBr is a promising vdW material that may serve as the platform for next-generation spintronics devices.

Spintronics

Systems

Spintronics exploits electron spin as an additional degree of freedom. Assume an MTJ system, where an inert layer separates a fixed FM layer from a "free" layer that may alternate between a parallel spin state and an antiparallel spin state to the fixed layer. As illustrated in Figure 2, the spin bands align well in the parallel state, enabling more frequent electron tunneling (Gallagher, 2006). When aligned antiparallel, the bands exhibit poor alignment, and electron tunneling is significantly reduced (Hemour, 2014). The resistance change is measured from the current across the MTJ and can encode a "1" or "0" bit.

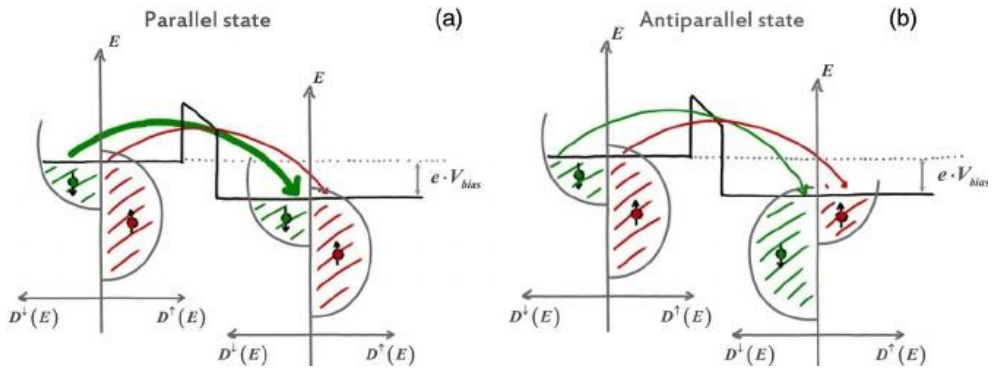

Figure 2: Tunneling resistivity in parallel and antiparallel MTJ systems.

Hemour, S., & Wu, K. (2014). Radio-Frequency Rectifier for Electromagnetic Energy Harvesting: Development Path and Future Outlook. Proceedings of the IEEE, 102, 1667–1691. https://doi.org/10.1109/JPROC.2014.2358691

The latest focus is on developing spin-orbit torque MRAM (SOT-MRAM). SOT-MRAM builds on spin-polarized current switching in STT-MRAM but incorporates a separate read-write path (Nguyen, 2024). The additional path bypasses restrictions of a single read-write path, which

is limited by a tradeoff between fast switching speeds and long-term endurance (Nguyen, 2024). Figure 3 schematically illustrates the difference.

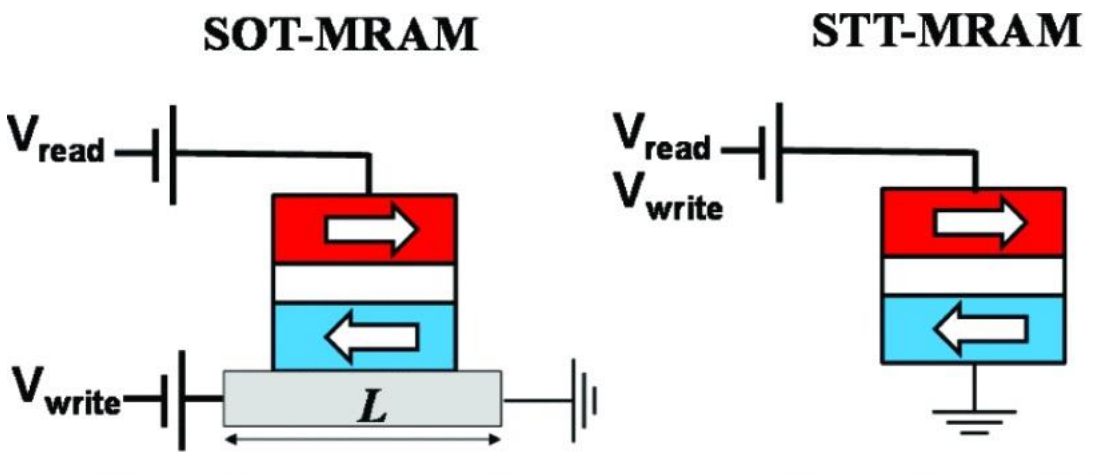

Figure 3: SOT-MRAM vs STT-MRAM.

SOT and STT MRAMs operation schemes. Two-terminal STT MRAM has the same path for read and write operations. Three-terminal SOT is capable of tuning read and write performance individually. Song, M. Y., Chen, K. L., Chen, K. M., Chang, K. T., Wang, I. J., Hsin, Y. C., Lin, C. Y., Ambrosi, E., Khwa, W.-S., Lu, Y. L., Hu, C. Y., Yang, S. Y., Li, S. H., Wei, J. H., Lee, T. Y., Wang, Y. J., Chang, M. F., Pai, C. F., & Bao, X. Y. (2023). High RA Dual-MTJ SOT-MRAM devices for High Speed (10ns) Compute-in-Memory Applications. 2023 International Electron Devices Meeting (IEDM), 1–4. https://doi.org/10.1109/IEDM45741.2023.10413832

Both the SOT and STT-MRAM incorporate a voltage source at the MTJ terminal to sense the MTJ state (Song, 2023). It is depicted as V_{read} in Figure 3. In STT, the free layer (blue) is written by sending a spin-polarized current in the V_{write} line to flip the spin (Song, 2023). If the DC current flows from the fixed layer to the free layer, the free layer spin aligns parallel to the fixed layer. If the DC current flows from the free layer to the fixed layer, the free layer aligns antiparallel (Song, 2023). The voltage required to write is significantly higher than the read voltage, owing to the lower efficiency of the STT system. Additionally, the STT system must wait for the current to dissipate before switching from read to write, which slows its speed. In the

SOT, the write line flips the free layer spin by passing through the SOT channel beneath it, rather than tunneling into it (Song, 2023).

The Field-Free Challenge

SOT-MRAM faces a field-free switching challenge that must be solved before large-scale commercialization. Current SOT-MRAM systems rely on an external FM field switcher to flip the free layer's spin (Li, 2016). As SOT-MRAM is continuously scaled down, this external field poses a parasitic magnetic-field risk to neighboring bits (Li, 2016). At the nanoscale, this unintentional flipping of neighboring bits impacts data integrity. This creates a lower limit on device size, severely impacting its applications. To efficiently scale down, a field-free SOT system must be developed.

The origin of this problem lies in the in-plane symmetry issue that arises when flipping the spin. The damping-like spin-orbit torque (DL-SOT) proportion is given by Equation 1 (Manchon, 2018)

$$\tau_{DL} \propto m \times (m \times \sigma), \quad (1)$$

where σ is the in-plane spin polarization generated by the spin-Hall effect in the heavy metal layer, and m is the perpendicular magnetization vector. The DL-SOT drives the magnetization vector from its initial out-of-plane state toward the film plane (Manchon, 2018). This can continue until the magnetization vector is essentially in-plane. At this point, the perpendicular anisotropy barrier is largely overcome (Yu, 2014). When the vector is rotated 90 degrees, now lying in-plane, the entire system has a mirror symmetry plane in the xz plane (Figure 4). Across the mirror symmetry plane, the induced current, J, and the in-plane spin polarization, σ, are unchanged. The magnetization vector, however, has an equal likelihood of being positive or

negative (Yu, 2014). This gives the SOT system two likely outcomes for the same initial input, making it non-deterministic.

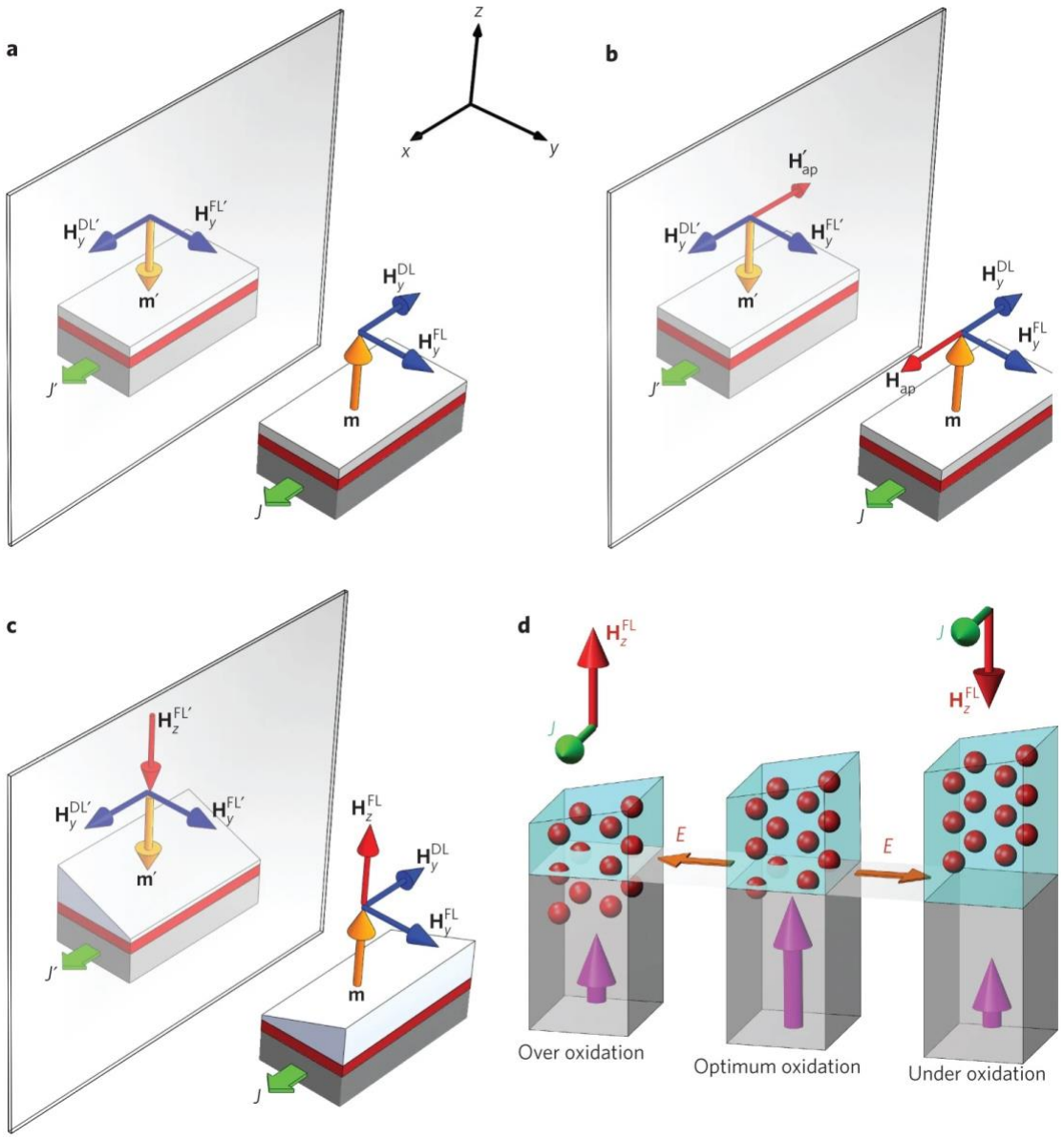

Figure 4: In-plane, mirror symmetry problem in deterministic switching of SOT systems.

a, Effective fields induced by current, and absence of deterministic out-of-plane switching, in a perpendicular magnetic structure that is symmetric with respect to the x–z plane. The typical stack structure is non-magnetic metal, ferromagnetic metal and oxide from bottom to top. The same direction of current allows for states with magnetization pointing up as well as down. The in-plane effective fields (H_y^{FL} and H_y^{DL}) are permitted due to the structural inversion asymmetry along the z axis. Blue arrows indicate H_y^{FL} and H_y^{DL} and their mirror reflections $H_y^{FL'}$ and $H_y^{DL'}$ with respect to the x–z plane. Note the difference between an external field H_{ap} and the damping-like field H_y^{DL}; the latter does not break the mirror symmetry with respect to the x–z plane as it

depends on m and changes sign when magnetization is reversed, while the former does break the aforementioned symmetry (see b). **b,** Symmetry with respect to the x–z plane is broken by applying an external magnetic field (H_{ap}) along the x direction. By fixing the direction of H_{ap} (either positive or negative with respect to the x axis), a unique perpendicular magnetization state can be chosen for each current direction. **c,** The new perpendicular effective field (H_z^{FL}) induced by the laterally asymmetric structure, and its mirror image ($H_z^{FL'}$). The presence of the new perpendicular effective field, induced by the lateral symmetry-breaking, uniquely determines the z component of the magnetization for a particular direction of current, thereby allowing deterministic switching without external magnetic fields. **d,** Schematic representation of the ferromagnet/oxide interface, illustrating its non-uniform oxygen content. The resulting non-uniform charge distribution may produce in-plane electric fields (E) along the interface, which in turn can contribute to the observed H_z^{FL}. Red spheres indicate oxygen atoms and perpendicular pink arrows correspond to the PMA in the magnetic layer.

Yu, G., Upadhyaya, P., Fan, Y., Alzate, J. G., Jiang, W., Wong, K. L., Takei, S., Bender, S. A., Chang, L.-T., Jiang, Y., Lang, M., Tang, J., Wang, Y., Tserkovnyak, Y., Amiri, P. K., & Wang, K. L. (2014). Switching of perpendicular magnetization by spin–orbit torques in the absence of external magnetic fields. Nature Nanotechnology, 9(7), 548–554. https://doi.org/10.1038/nnano.2014.94

To make this deterministic, the mirror symmetry plane must be broken. Traditionally, this was done by applying an external in-plane magnetic field along the direction of the current to tilt more favorably toward one outcome (Li, 2016). This comes with the parasitic magnetism issues previously discussed. Field-free switching is the proposed solution (Li, 2016). AFM materials offer a promising pathway to achieve this. Unlike a global external field, CrSBr generates a localized, in-plane exchange bias right at the interface with the perpendicular ferromagnet (Cham, 2024). This internal bias breaks mirror symmetry, creates slightly canted magnetization states, and favors one end state. The result is reliable, deterministic switching using only electrical current, with no external magnets required.

CrSBr

CrSBr is a strong contender as the AFM material for SOT-MRAM systems. It belongs to the orthorhombic *Pmmn* space group (Lee, 2021). It is a vdW material which holds its magnetic ordering down to the 2D limit (Ziebel, 2024). Like other 2D magnetic materials, this makes it

highly tunable by external fields (Shi, 2025). The bilayer structure of CrSBr is shown in Figure 5.

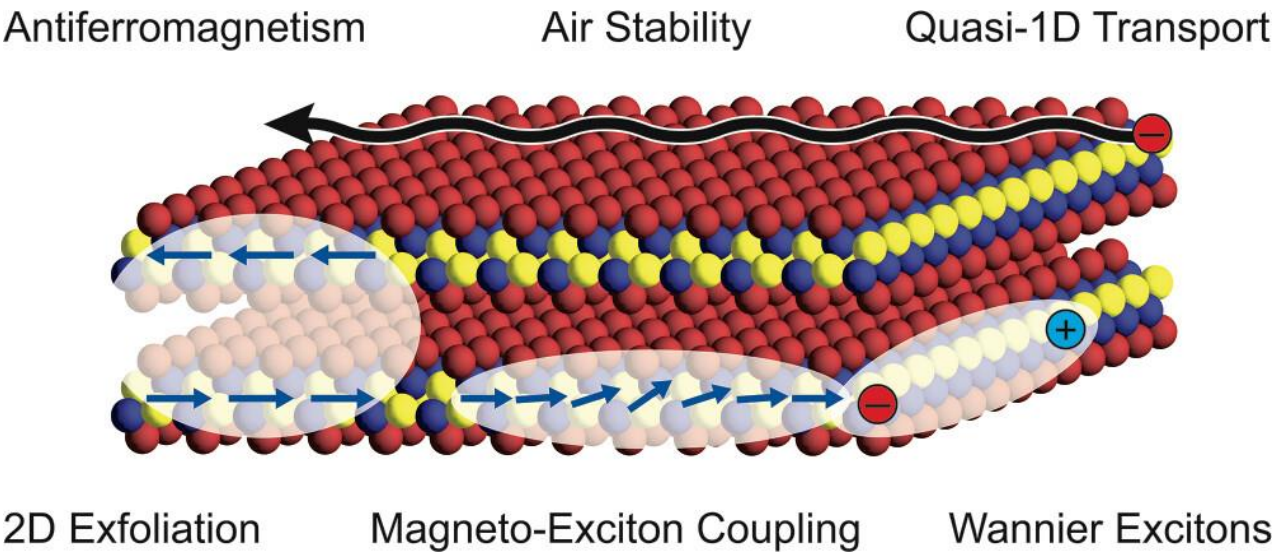

Figure 5: CrSBr bilayer with blue arrows indicating the magnetic moment of each layer. Red atoms represent Br, yellow atoms represent S, and blue atoms represent Cr, Ziebel, M. E., Feuer, M. L., Cox, J., Zhu, X., Dean, C. R., & Roy, X. (2024). CrSBr: An Air-Stable, Two-Dimensional Magnetic Semiconductor. Nano Letters, 24(15), 4319–4329. https://doi.org/10.1021/acs.nanolett.4

A covalently bonded Cr-S backbone forms the crystal structure across a layer. This backbone is insulated by Br on both sides, which holds together adjacent layers through vdW interactions (Ziebel, 2024). The crystal structure displays A-type antiferromagnetism, resulting in a spin direction that is consistent throughout a layer, but opposite between adjacent layers (Shi, 2025).

CrSBr is an attractive candidate for electronic systems because it exhibits a high degree of stability. Unlike similar 2D magnetic materials which degrade or oxidize in air, CrSBr's chemistry remains stable in ambient conditions, simplifying device fabrication as extensive encapsulation techniques are not required (Shi, 2025). Additionally, CrSBr has a high Néel temperature of 132 K, reducing the need for supercooling (Ziebel, 2024). The intralayer

ferromagnetic ordering is maintained up to a Curie temperature of 142 K (Shi, 2025). Each of these factors make CrSBr more resilient after integration in an electronic device.

The magnetic character of CrSBr is also favorable to SOT systems. In bilayer or bulk structures, the A-type AFM produces no net magnetic moment. As previously discussed, this prevents crosstalk and allows for significantly smaller devices (Cham, 2024). Additionally, its Néel vector lies in-plane (Shi, 2025). When interfaced with another material, this allows for the exchange biasing necessary to break the mirror symmetry (Li, 2016).

CrSBr's electronic properties are also favorable for an SOT use case. It functions as a semiconducting material with a sizeable band gap of 1.5-2 eV (Biktagirov, 2025). In an SOT device, the CrSBr would sit atop a heavy metal with an active current for write capabilities (Song, 2023). Because of its band gap, there is little risk of current leakage from the heavy metal through the CrSBr layer. This keeps the torque generation highly efficient as the current remains in the heavy metal where the spin Hall effect is strongest. This also prevents unwanted spin flip scattering to occur, maintaining the pinning layer with a strong exchange bias (Ziebel, 2024).

Finally, the layered structure of CrSBr is beneficial for creating heterostructures with other vdW materials. Monolayer and few-layer flakes of this material are achievable from Scotch tape exfoliation techniques (Ziebel, 2024). The exposed surface presents an atomically sharp, clean interface with no lattice mismatch strain or dangling bonds (Cham, 2024). This allows for mechanical stacking of CrSBr with other vdW materials, like graphene, in SOT systems, presenting more advanced opportunities for creative materials engineering.

DFT Computations Using VASP

DFT calculations were performed to obtain the band structures of CrSBr bulk. These band structures provide key insights into the material's electronic states and spin-dependent properties. By utilizing these insights, the effectiveness of CrSBr in a spintronic system will be understood.

For this investigation, VASP was utilized as the computational tool. VASP is a DFT software package based on the Kohn-Sham (KS) theory (Saßnick, 2021). In the KS-DFT framework, the many-body problem pertaining to the electron network is effectively approximated by mapping the "system into an auxiliary system of non-interacting electrons with the same density as the fully interacting one" (Saßnick, 2021). This allows an accurate approximation of the system's ground-state density by solving the Kohn-Sham single-particle equation (Kohn, 1965).

$$\left[-\frac{1}{2}\nabla^2 + v_s(\boldsymbol{r})\right]\varphi_i(\boldsymbol{r}) = \epsilon_i^{KS}\varphi_i(\boldsymbol{r}) \tag{2}$$

The above single particle equation provides both the KS wavefunction of the particle in the form of the eigenfunction, $\varphi_i(\boldsymbol{r})$, and the KS energy per particle in the form of the eigenvalue, ϵ_i^{KS} (Kohn, 1965). VASP employs a self-consistent field loop to iteratively solve this equation in tandem with the effective potential per particle below (Saßnick, 2021).

$$v_s(\boldsymbol{r}) = v_{ext}(\boldsymbol{r}) + v_H(\boldsymbol{r}) + v_{xc}(\boldsymbol{r}) \tag{3}$$

$v_{ext}(\boldsymbol{r})$ accounts for the electron-nuclear interaction, $v_H(\boldsymbol{r})$ the Hartree potential, and $v_{xc}(\boldsymbol{r})$ the exchange-correlation potential (Saßnick, 2021). The exchange-correlation potential is unknown and must be approximated using a functional in VASP.

The generalized gradient approximation (GGA) Perdew-Burke-Ernzerhof (PBE) method was used to account for the electronic exchange-correlation effects. The $v_{xc}(\boldsymbol{r})$ depends on both the local density and reduced gradient (Saßnick, 2021). This approximation produces reliable results for geometry optimizations as it mainly relies on balancing the attractive and repulsive forces. It is also considerably computationally inexpensive, further reinforcing its status as the base case functional for geometry optimizations. However, GGA-PBE functional approximations lead to excess charge delocalization and self-interaction error, resulting in underestimation of band gaps, shallow conduction bands, and inaccurate band alignments (Vignesh, 2024). While efficient for geometry optimizations, an alternative functional is required to accurately approximate band structures, particularly for complex electromagnetic materials like CrSBr.

Hybrid functionals are used to address the shortcomings of the GGA-PBE functional. This class of functionals uses the Hartree potential to supplement the PBE-exchange-correlation potential. The Heyd–Scuseria–Ernzerhof (HSE06) hybrid functional is widely used. The HSE06 functional splits the electron-electron interaction parameter into two parts: a short-range and long-range (Saßnick, 2021). The long-range parameter is consistent with the PBE functional calculation, while the short-range parameter is 75% derived from the PBE functional and 25% from the Hartree-Fock exchange (Saßnick, 2021). This corrects much of the self-interaction error, leading to a more electronically accurate effective potential per particle. While yielding more accurate electrical characteristics, the hybrid functional is significantly more computationally expensive than the PBE functional. Thus, its use is often reserved for

complicated materials that are severely misrepresented by the PBE functional or when precise electrical and spin properties are required.

Methods

Based on the information discussed above, a systematic approach was created and replicated for each of the three structures explored in this report. A process overview will be presented, and then the specifics for each crystal structure will follow. To begin, the primitive unit cell structure for CrSBr was obtained as a POSCAR from the Materials Project. Manipulations were performed to the base structure to simulate crystal variants and defects. The Monkhorst-Pack k-point generation scheme was utilized to create a 12x8x2 mesh. With the base structure, a geometry optimization was performed utilizing the GGA-PBE functional in VASP version 6.4.3. The relaxation was spin polarized with an energy cutoff of 520 eV. It utilized tetrahedron method smearing with Blöch corrections and a max smearing width of 0.05 eV. vdW interactions were accounted for using the DFT-D3 method with Becke-Johnson damping function. The convergence criterion for self-consistency was set to a differential energy of 10^{-6} eV with a limit of 60 iterations per ionic step. The conjugate gradient (CG) algorithm was used for relaxation, with a step size of 0.2 for ionic relaxation. For the FM case, the initial magnetic moment of each Cr was 3 and all other atoms 0.6. For the AFM case, one Cr was set at 3 and the other at -3.

The relaxed structure was parsed through to a static calculation of the material utilizing the HSE06 hybrid functional to generate wavefunctions and charge densities. It utilized the same energy cutoff. The functional utilized a screening parameter of 0.2 $Å^{-1}$ and 25% exact Hartree-Fock exchange. The calculation used a damped algorithm with a time step of 0.4. It was

performed as a single-point calculation. Spin polarization was enabled to account for the magnetic properties of CrSBr. The maximum number of self-consistency iterations was increased to 100, and the convergence criterion was reduced to 10^{-5} eV. Gaussian smearing with a width of 0.05 eV was used for Brillouin zone integration.

After obtaining static outputs, the irreducible Brillouin zone k-points file (IBZKPT) is used in conjunction with the crystal structure to generate a high symmetry k-point path across the Brillouin zone. This was realized using the sumo package. The band calculation was configured as non-self-consistent with symmetry off. Charge density and wavefunctions were read from the preceding static calculation. Spin polarization was maintained with orbital projected outputs enabled. The band calculation was ultimately performed using the hybrid functional, HSE06. The bandplot and dosplot functions of the sumo package were then used to plot the band structure and density of states plot.

The first band calculation was performed on FM CrSBr, while the second was performed on antiferromagnetic AFM CrSBr. The difference between these two was simply the magnetic moment applied to the two base chromium atoms in each cell: the FM having equal moments, while the AFM had opposite. A H-doped CrSBr was also investigated. An inferred estimate was made to place the hydrogen in the center of the cell and then geometry optimization found the idealized structure.

Results

Geometry Optimization

After completing all three simulations, the first step was to compile the results of the geometry relaxation. The results are shown in Table 1.

Table 1: Optimized lattice parameters for CrSBr variants.

CrSBr Variant	a (Å)	b (Å)	c (Å)
FM	3.513	4.690	7.920
AFM	3.509	4.719	7.861
H-doped AFM	3.654	4.993	7.145

Literature reports lattice parameters for the FM and AFM bulk crystal of a = 3.50 – 3.55, b = 4.74 – 4.82, and c = 7.96 – 8.00, consistent with the lattice parameters found in this study (Rudenko, 2023; Ziebel, 2024). For the H-doped lattice, the hydrogen consistently bonded with the sulfur atoms in the relaxed structure. Attempts were made to determine if there were other favorable structures for H, but VASP results favored the structure in Figure 6.

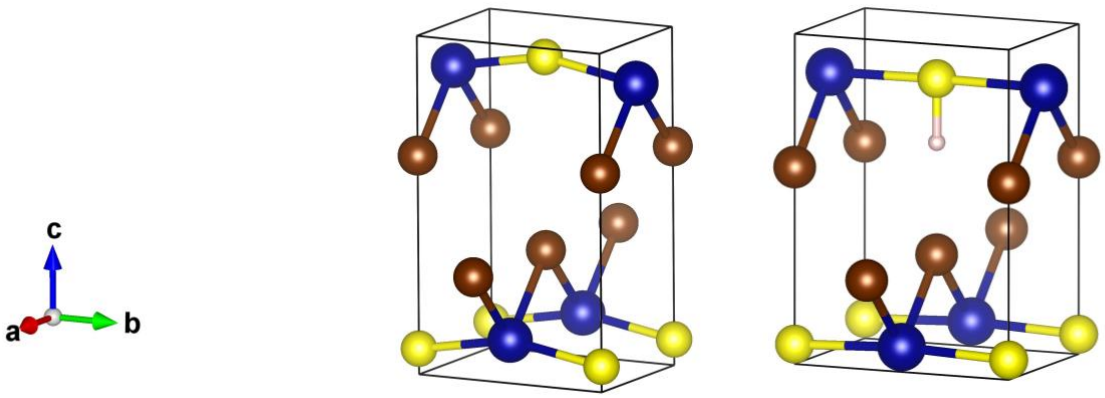

Figure 6: Molecular structure of AFM CrSBr (left) and H-doped AFM CrSBr (right).

The differences between the FM and AFM bulk lattice constants were small. This is potentially useful for spintronics systems, as interlayer magnetism switching can be performed without altering the overall structure. For the H-doped variant, the in-plane lattice is slightly expanded while the vdW gap is compressed. With the addition of the extra atom, it would be expected that the c-axis would expand, thus, it is somewhat unexpected to observe lattice contraction. This observation could allow potential manipulations of the material.

The bond lengths in each structure are shown in Table 2. Bond lengths are relatively unchanged between the FM and AFM variants. In the H-doped variant, both the Cr-S and Cr-Br bonds are stretched to accommodate the hydrogen atom. In the AFM and FM variants, all like atom bonds have the same length. In the H-doped variant, there is a slight difference between the length of the bonds in the top surface (+c direction in Figure 6) and bottom surface (-c direction in Figure 6). For both the Cr-S and Cr-Br bonds in the H-doped variant, the bottom surface bond lengths are shorter than the top surface bonds.

Table 2: CrSBr variant bond lengths.

CrSBr Variant	Bond		
	Cr-S (Å)	**Cr-Br (Å)**	**S-H (Å)**
FM	2.385	2.500	
AFM	2.394	2.498	
H-doped AFM	2.496 (top surface) 2.499 (bottom surface)	2.552 (top surface) 2.511 (bottom surface)	1.377

The bond angles were also calculated and reported in Table 3.

Table 3: CrSBr variant bond angles.

CrSBr Variant	Bond		
	Br-Cr-Br (°)	**Br-Cr-S (°)**	**Cr-S-Cr (°)**
FM	89.241	97.466	158.963
AFM	89.238	96.923	160.500
H-doped AFM	91.419 (top surface) 93.372 (bottom surface)	90.374 (top surface) 91.667 (bottom surface)	178.929

Literature results for AFM CrSBr report the Br-Cr-Br ,and no significant change in bond angle occurs between the AFM and FM variants. In the H-doped variant, the Cr-S-Cr is flattened to nearly 180°, while the other bonds widen slightly to accommodate this flattening. Again, a discrepancy appears between the angles on the top surface and bottom surface of the H-doped variant to accommodate the extra volume of the H.

Static Calculation

Static calculation results were used to compare the magnetic properties of each crystal structure. The magnetic moments of each formula unit in the unit cell are summarized in Table 4.

Table 4: Magnetic moments per formula unit for CrSBr variants.

Formula Unit	CrSBr Variant		
	FM (μ_B)	AFM (μ_B)	H-doped AFM (μ_B)
Cr	3.075	3.003	3.392
Cr	3.075	-3.002	-3.370
S	-0.168	0.027	-0.004
S	-0.168	-0.027	-0.046
Br	-0.030	-0.029	-0.043
Br	-0.030	0.029	0.037
H			0.008
Total Per Cell	**5.754**	**0.000**	**-0.025**

The computational results from the ferromagnetic CrSBr variant show full alignment. There is clear net ferromagnetism in both layers. In the AFM case, the results show the magnetic moments between two neighboring layers are equal in magnitude and opposite. There is perfect cancellation between the constituents, leading to a net zero magnetic moment. This aligns with CrSBr's A-type antiferromagnetism character (Ziebel, 2024). In H-doped CrSBr, the perfect AFM symmetry is slightly disrupted but largely preserved by the dopant.

Band Calculation

Band calculations were performed to generate three distinct band structures: FM CrSBr, AFM CrSBr, and H-doped CrSBr variant. The band structure of FM CrSBr is shown in Figure 7.

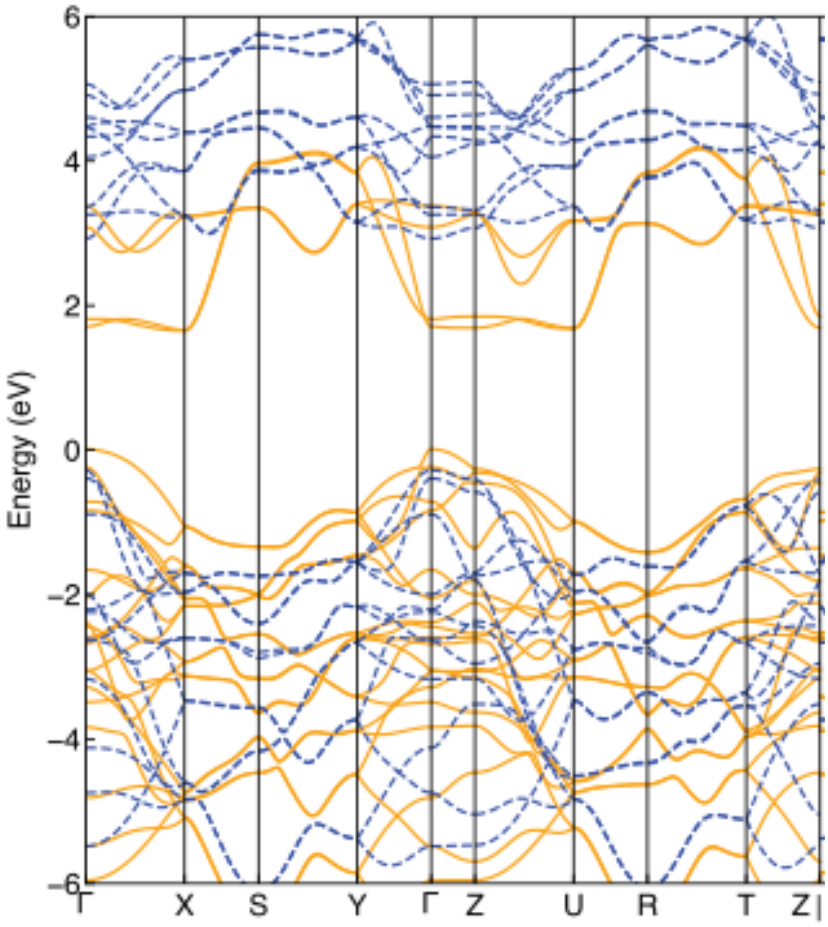

Figure 7: Band structure of ferromagnetic CrSBr.

In the ferromagnetic material, two distinct sets of bands are present due to spin-splitting. Yellow, solid curves in the plot represent the spin-up bands. These are called the majority bands and represent the electrons whose spin is aligned parallel to the net magnetization of the material. Blue, dashed curves represent the spin-down, minority bands. The spin on electrons in these bands is aligned antiparallel to the net magnetization of the material. In this plot, the band gap

occurs at the Γ position and is approximately 1.8-1.9 eV. A significant exchange shift occurs in the conduction band, indicating a 1-2 eV more favorable exchange energy for spin-up electrons.

In addition to the band structure plot, the density of states plot was generated to aid in the material analysis and is shown in Figure 8. Spin-up bands are plotted above the midpoint line while spin-down bands are plotted below.

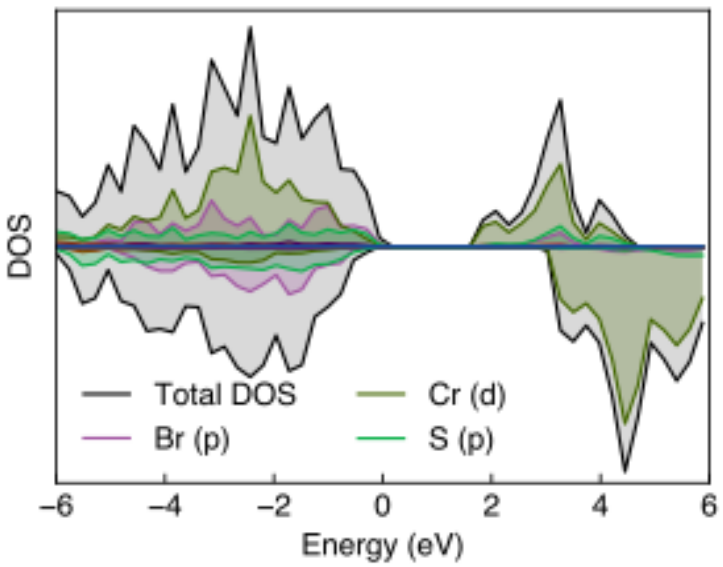

Figure 8: Density of states (DOS) for ferromagnetic CrSBr.

The DOS plot clearly shows semiconducting nature and reaffirms the band gap of approximately 1.8-1.9 eV. There is strong asymmetry between the majority and minority bands, reinforcing the ferromagnetic character observed in the band plot. Majority bands fill up more in the valance band region while the minority electrons are pushed higher into the conducting region. Significant exchange splitting occurs in the conduction band.

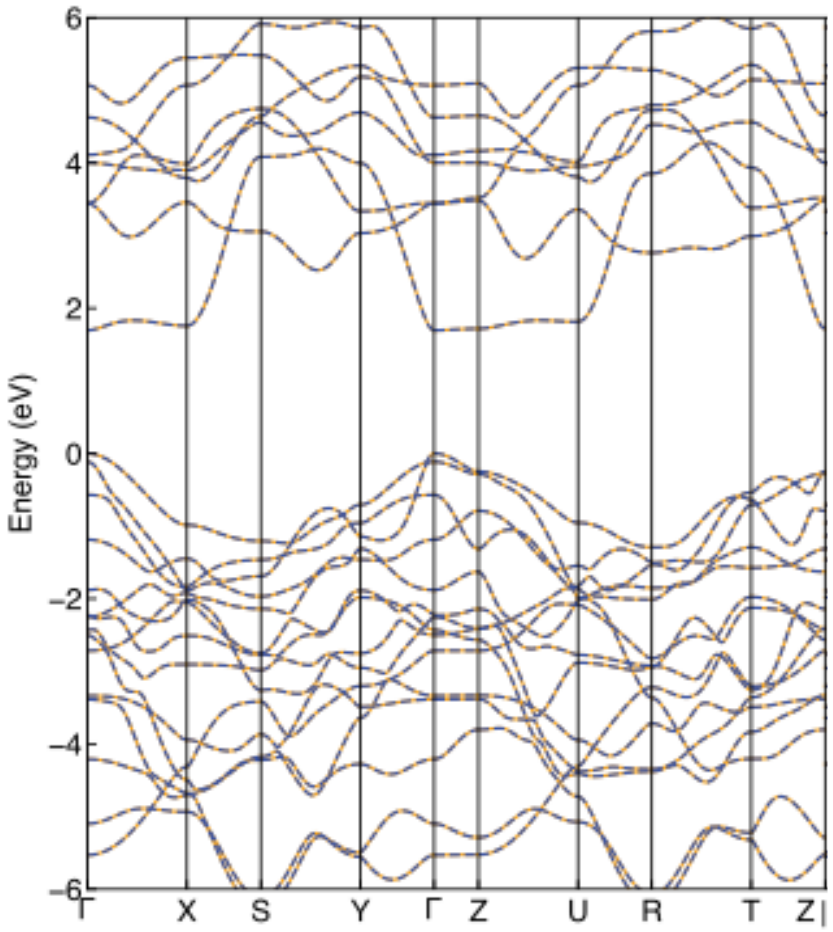

Figure 9: Band structure for AFM CrSBr.

The AFM variant is highly reflective of the ferromagnetic band structure, however, no spin-splitting occurs. Coincident majority and minority spin bands show complete degeneracy, leading to the net zero magnetic moment. The band gap remains at the Γ position and maintains the approximately 1.8-1.9 eV value.

The density of states plot in Figure 10 supports this conclusion. It demonstrates perfect symmetry, reinforcing the net zero magnetic moment seen in the band structure. Cr (d-band) displays the dominant character, especially in the conduction band. The density distribution

across the valence bands is uniform. It is interesting to see that Cr (s) makes some contributions, albeit minor, to the valence band density.

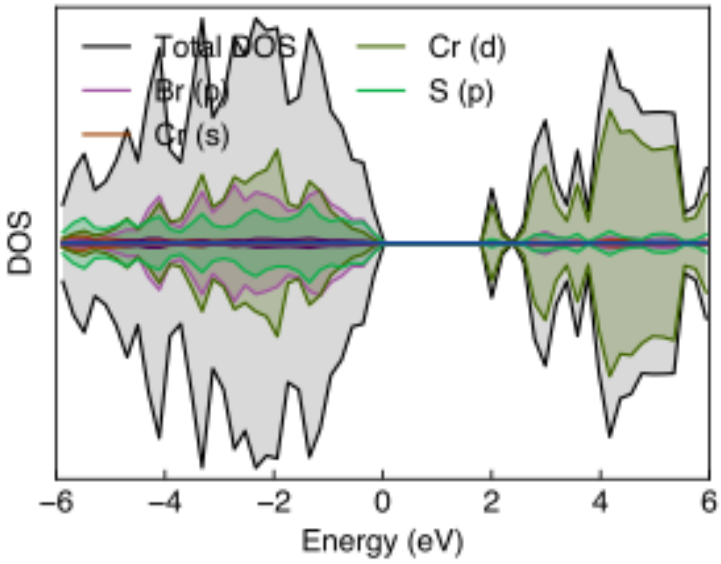

Figure 10: Density of states (DOS) plot for AFM CrSBr.

The H-doped AFM band structure (Figure 11) exhibits significant differences between the AFM and FM variants. Spin-up and spin-down bands are more degenerate than the FM case, but less than the AFM case, especially in the valence band region. There is exchange splitting between the bands, which is most evident in the conduction band. This would cause a slight magnetic moment, which agrees with the results of Table 2. The band gap is no longer present, indicating that the hydrogen transitioned the semiconducting nature to a conductive one. Interestingly, the Fermi energy has been shifted from 0 to just above -2 eV and the plot shows the valence band shifting down, away from the conduction band direction.

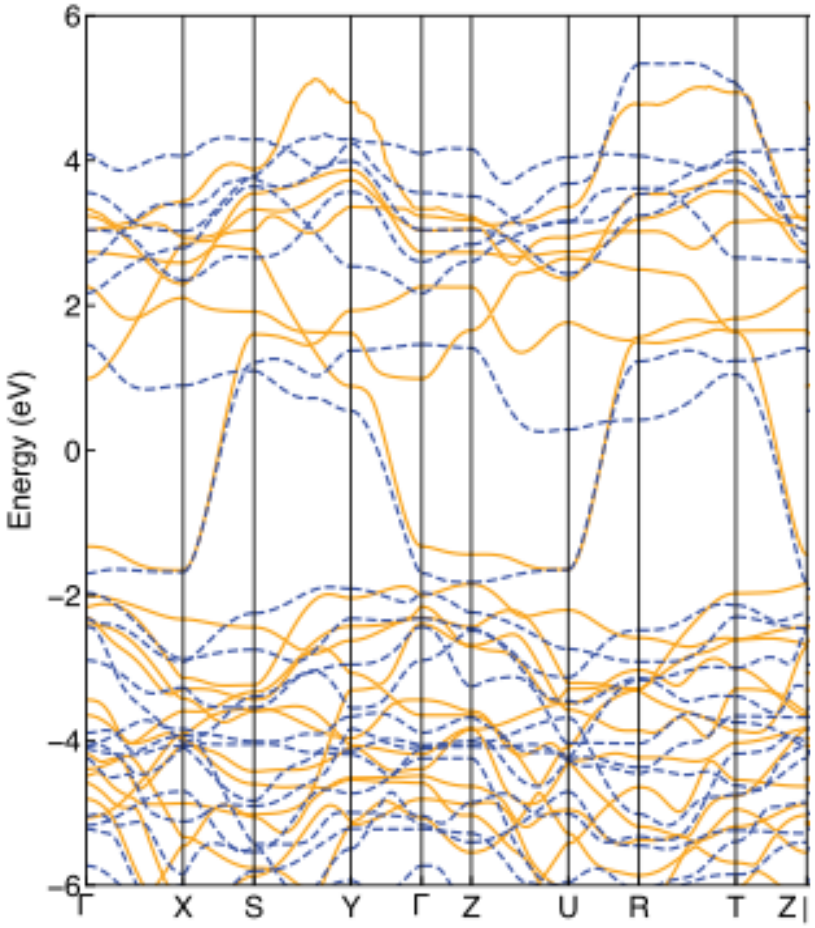

Figure 11: Band structure for the H-doped AFM CrSBr variant.

To further investigate the doping effect, the band plot was compared to the density of states plot in Figure 12. The intermediary degeneracy in the valance band region observed in the band plot is echoed in the DOS plot by some symmetry below the fermi energy. There is some minor exchange splitting from Cr (d-band) in the valence band, but it is mostly offset by the other constituents and has a negligible effect on the total DOS. More exchange splitting occurs in the conduction band, almost entirely driven by Cr. Like the band structure, the fermi energy shift away from zero is observed.

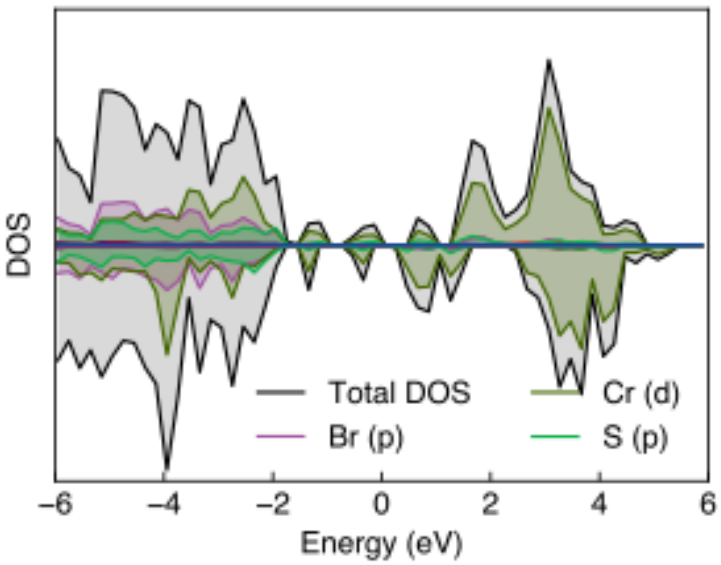

Figure 12: Density of states plot for H-doped AFM CrSBr.

Discussion

The agreement of the lattice parameters, bond lengths, and bond angles with literature values gives credibility to the computational method and results, particularly the use of the GGA-PBE functional, DFT-D3 method, and spin-polarized relaxation. Minimal differences between the FM and AFM configurations suggest that the lattice structure is only weakly influenced by the magnetic ordering. For the H-doped AFM variant, expansions of the a and b lattice parameters were expected as the additional atom in the lattice increases the volume. It was hypothesized that the c parameter would also experience expansion, yet the c parameter contracted by 9.1%. The lengthening of the Cr-S bonds, along with the flattening of the Cr-S-Cr angle in the H-doped variant explains this contraction. To make space for the hydrogen in the center of the lattice, the Br must expand away from the center, forcing the flattening of the Cr-S-Cr bond angle which decreased the overall c parameter.

A unique artifact from the geometry optimization was that the top surface and bottom surface of the H-doped variant had different bond lengths and angles for the same bond types. Similarly to how the symmetry is broken in the band structure when doped, it is hypothesized that the electrostatic asymmetry from the hydrogen leads to slight geometric asymmetry between the top surface and bottom surface. Further testing is required for clarity in this regard.

In the static calculation, the H-doped variant had its magnetic symmetry broken but still had a near zero total moment. This result is interesting as it shows the introduction of hydrogen does not break the AFM ordering of CrSBr, even when doped at such high levels. Hydrogen causes a disruption in the symmetry but not a transition from an AFM state to an FM one. The imbalance in the magnetic moments reflects the asymmetry in the geometry optimization, as the hydrogen creates a local imbalance in the top surface of the lattice structure. Importantly, the

ability of CrSBr to maintain its zero net magnetic moment, even when doped, is highly desirable for MRAM devices. As the pinning layer in the SOT systems, it is essential that CrSBr minimize crosstalk in dense arrays. These results affirm the robustness of CrSBr against mild defects during device fabrication. It also opens doors to opportunities for defect engineering in CrSBr in these systems.

The band calculations revealed distinct electronic behavior across the three variants. Both the FM and AFM variants had a band gap of 1.8-1.9 eV, indicating the spin layering has no impact on the semiconducting nature. In the FM phase, spin-splitting is observed with the spin-up bands shifted to lower energies than the spin-down bands, especially in the conduction band. The DOS plot confirms this asymmetry. Furthermore, the minority bands have reduced density in the valence band relative to the majority bands, but increased density in the conducting band relative to the majority bands. This results in strong exchange splitting. In contrast, the AFM variant has perfect symmetry between spin bands. The degeneracy gives rise to the zero net magnetic moment, a necessary property for field-free systems.

The H-doped variant band structure was significantly different from the AFM and FM. Note that this level of hydrogen doping is significantly higher than would be typical from manufacturing defects or intentional doping. The high level, however, allows for more insights into its effects. H-doping eliminated the band gap, transforming CrSBr from a semiconductor to a metal. Additionally, the fermi level decreases by 2 eV. Similar studies have shown that hole-doping (p-type) leads to the reverse effect (Han, 2023). This may provide some insight into the character of the hydrogen in this system. The shift in the Fermi energy may indicate that hydrogen acts as an n-type dopant, donating electrons to the system. The DOS plots also show that the donated electrons from the hydrogen are likely filling spots in the previous band gap

space, as three small spikes are seen between the conduction and valance bands. Surprisingly, the AFM character was largely maintained with only a small magnetic moment produced in the doped case.

In device application, the H-doped variant would largely maintain the field-free advantage, but the pure AFM variant is still preferred for its perfect degeneracy. The closure of the band gap would be the most disadvantaged result of the doping. As discussed in the CrSBr section, the semiconducting nature of the pure AFM variant prevents current leakage in the SOT-MRAM system. If the CrSBr instead exhibited metallic nature, the some current from the write line would likely divert into the CrSBr pinning layer, reducing efficiency (Song, 2023). Depending on the strength of the current in the write line, this could also impact the spin states, threatening the reliability as a pinning layer. Practically, sparse doping may be useful to fine tune band gap properties, but doping at the level performed in this investigation would be undesirable. It does highlight the importance of controlling hydrogen exposure during synthesis and device fabrication.

Overall, the band calculations are consistent with the geometry optimization and static results. Hydrogen causes local perturbations that break symmetry, but the AFM character is maintained. CrSBr is robust in maintaining its magnetic character, but its electronic properties are highly sensitive to doping. While hydrogen may not be a desirable dopant for these applications, the sensitivity to dopants is promising for future band gap engineering efforts. CrSBr is a strong candidate for SOT-MRAM devices but the system as a whole still faces challenges before practical production is achievable.

Future Research and Recommendations

While this investigation revealed interesting properties of bulk CrSBr and the effects of doping, several extensions must be explored to incorporate the findings into actual SOT systems. First, replicating this computational experiment in a laboratory to confirm the results would uphold the results found here. Future research should also investigate the bilayer systems rather than just the bulk. In ideal systems, the bilayer represents the thinnest, and most scalable, design while still retaining the field-free advantage of an AFM system. While the bulk is highly robust in maintaining its AFM properties, it would be interesting to see if the bilayer maintains its magnetic and electronic characteristics with a large write current beneath it. The bulk has enough insulating layers to protect the overall AFM characteristic, but this may not hold up with just the bilayer.

Performing deeper analyses on the results would be beneficial, specifically using tools like Bader charge analysis. Bader charge analysis would quantify the level, distribution, and direction of the charge effects in the cell. It would help determine which orbitals are hybridizing at the interface and having the most profound effect on the exchange field. This would assist in tuning dopants to best control the biasing on the SOT system.

Finally, an investigation of a stacked, vdW interface between a thin CrSBr layer and graphene could provide insight for future breakthroughs. There has been interest in creating a heterostructure of CrSBr and graphene that could manipulate the Neel vector by electrostatically tuning the spin current (Yang, 2024). The graphene would act as the highly conducting layer while the CrSBr induces an exchange field that creates spin-polarized carriers in graphene (Yang, 2024). This could create a more efficient SOT system that is voltage tunable as opposed

to current tuned. Modeling these systems would provide insight on the interface and how the heterostructure system characteristics respond in the SOT environment.

References

Baibich, M. N., Broto, J. M., Fert, A., Van Dau, F. N., Petroff, F., Etienne, P., Creuzet, G., Friederich, A., & Chazelas, J. (1988). Giant Magnetoresistance of (001)Fe/(001)Cr Magnetic Superlattices. Physical Review Letters, 61(21), 2472–2475. https://doi.org/10.1103/PhysRevLett.61.2472

Binasch, G., Grünberg, P., Saurenbach, F., & Zinn, W. (1989). Enhanced magnetoresistance in layered magnetic structures with antiferromagnetic interlayer exchange. Physical Review B, 39(7), 4828–4830. https://doi.org/10.1103/physrevb.39.4828

Biktagirov, T., Schmidt, W. G., Schiller, K. J., Capra, M., Nitschke, J. E., Sternemann, L., Arndt, M. S., Zamborlini, G., Isaeva, A., & Cinchetti, M. (2025). Intrinsic defects as a source of n-type conductivity in CrSBr. Npj 2D Materials and Applications, 9(1), 106. https://doi.org/10.1038/s41699-025-00640-7

Cham, T. M. J., Dorrian, R. J., Zhang, X. S., Dismukes, A. H., Chica, D. G., May, A. F., Roy, X., Muller, D. A., Ralph, D. C., & Luo, Y. K. (2024). Exchange Bias Between van der Waals Materials: Tilted Magnetic States and Field-Free Spin–Orbit-Torque Switching. Advanced Materials, 36(13), 2305739. https://doi.org/10.1002/adma.202305739

Chen, B., Zeng, M., Khoo, K. H., Das, D., Fong, X., Fukami, S., Li, S., Zhao, W., Parkin, S. S. P., Piramanayagam, S. N., & Lim, S. T. (2023). Spintronic devices for high-density memory and neuromorphic computing – A review. Materials Today, 70, 193–217. https://doi.org/10.1016/j.mattod.2023.10.004

Gallagher, W. J., & Parkin, S. S. P. (2006). Development of the magnetic tunnel junction MRAM at IBM: from first junctions to a 16-Mb MRAM demonstrator chip. IBM Journal of Research and Development, 50(1), 5–23. https://doi.org/10.1147/rd.501.0005

Han, R., Xue, X., & Yan, Y. (2023). Hole-Doping-Induced Perpendicular Magnetic Anisotropy and High Curie Temperature in a CrSX (X = Cl, Br, I) Semiconductor Monolayer. Nanomaterials, 13(24). https://doi.org/10.3390/nano13243105

Hemour, S., & Wu, K. (2014). Radio-Frequency Rectifier for Electromagnetic Energy Harvesting: Development Path and Future Outlook. Proceedings of the IEEE, 102, 1667–1691. https://doi.org/10.1109/JPROC.2014.2358691

Huang, K., Zhao, R., Ning, N., & Lian, Y. (2014). A low power localized 2T1R STT-MRAM array with pipelined quad-phase saving scheme for zero sleep power systems. IEEE Transactions on Circuits and Systems I: Regular Papers, 61(9), 2614–2623. https://doi.org/10.1109/TCSI.2014.2333361

International Energy Agency. (2025). Data centre electricity consumption by region, Base Case, 2020-2030 [Chart]. https://www.iea.org/data-and-statistics/charts/data-centre-electricity-consumption-by-region-base-case-2020-2030

Kohn, W., & Sham, L. J. (1965). Self-Consistent Equations Including Exchange and Correlation Effects. Physical Review, 140(4A), A1133–A1138. https://doi.org/10.1103/PhysRev.140.A1133

Lawson, A. J., Offutt, M. C., & Zhu, L. (2026). Data Centers and Their Energy Consumption: Frequently Asked Questions. Congress.gov. https://www.congress.gov/crs-product/R48646

Lee, K., Dismukes, A. H., Telford, E. J., Wiscons, R. A., Wang, J., Xu, X., Nuckolls, C., Dean, C. R., Roy, X., & Zhu, X. (2021). Magnetic Order and Symmetry in the 2D Semiconductor CrSBr. Nano Letters, 21(8), 3511–3517. https://doi.org/10.1021/acs.nanolett.1c00219

Li, X., & Yang, J. (2016). First-principles design of spintronics materials. National Science Review, 3(3), 365–381. https://doi.org/10.1093/nsr/nww026

Manchon, A., Miron, I., Jungwirth, T., Sinova, J., Zelezny, J., Thiaville, A., Garello, K., & Gambardella, P. (2018). Current-induced spin-orbit torques in ferromagnetic and antiferromagnetic systems. Review of Modern Physics, 91. https://doi.org/10.1103/RevModPhys.91.035004

Nguyen, V. D., Rao, S., Wostyn, K., & Couet, S. (2024). Recent progress in spin-orbit torque magnetic random-access memory. Npj Spintronics, 2(1), 48. https://doi.org/10.1038/s44306-024-00044-1

Nobel Prize Outreach. (2007). Popular Information. NobelPrize.Org. https://www.nobelprize.org/prizes/physics/2007/popular-information/

Ornes, S. (2013). Giant Magnetoresistance. Proceedings of the National Academy of Sciences, 110(10), 3710–3710. https://doi.org/10.1073/pnas.1302494110

Rudenko, A. N., Rösner, M., & Katsnelson, M. I. (2023). Dielectric tunability of magnetic properties in orthorhombic ferromagnetic monolayer CrSBr. Npj Computational Materials, 9(1), 83. https://doi.org/10.1038/s41524-023-01050-3

Saßnick, H.-D., & Cocchi, C. (2021). Electronic structure of cesium-based photocathode materials from density functional theory: Performance of PBE, SCAN, and HSE06 functionals. Electronic Structure, 3(2), 027001. https://doi.org/10.1088/2516-1075/abfb08

Shi, J., Wang, D., Jiang, N., Xin, Z., Zheng, H., Shen, C., Zhang, X., & Liu, X. (2025). Giant Magneto-Exciton Coupling in 2D van der Waals CrSBr. ACS Nano, 19(33), 29977–29987. https://doi.org/10.1021/acsnano.5c00407

Song, M. Y., Chen, K. L., Chen, K. M., Chang, K. T., Wang, I. J., Hsin, Y. C., Lin, C. Y., Ambrosi, E., Khwa, W.-S., Lu, Y. L., Hu, C. Y., Yang, S. Y., Li, S. H., Wei, J. H., Lee, T. Y., Wang, Y. J., Chang, M. F., Pai, C. F., & Bao, X. Y. (2023). High RA Dual-MTJ SOT-MRAM devices for High Speed (10ns) Compute-in-Memory Applications. 2023 International Electron Devices Meeting (IEDM), 1–4. https://doi.org/10.1109/IEDM45741.2023.10413832

Vignesh, D., & Rout, E. (2024). Custom hybrid activation function over delocalization error for gap state predictions of A2CeZrO6 (A = Ba2+, Sr2+, Ca2+, Mg2+) proton conductors: A

first-principles and machine learning approach. The Journal of Physical Chemistry C, 128(39), 16684–16700. https://doi.org/10.1021/acs.jpcc.4c03379

Wu, H., Zhang, J., Cui, B., Razavi, S. A., Che, X., Pan, Q., Wu, D., Yu, G., Han, X., & Wang, K. L. (2022). Field-free approaches for deterministic spin–orbit torque switching of the perpendicular magnet. Materials Futures, 1(2), 022201. https://doi.org/10.1088/2752-5724/ac6577

Yang, B., Bhujel, B., Chica, D. G., Telford, E. J., Roy, X., Ibrahim, F., Chshiev, M., Cosset-Chéneau, M., & Wees, B. J. van. (2024). Electrostatically controlled spin polarization in Graphene-CrSBr magnetic proximity heterostructures. Nature Communications, 15(1), 4459. https://doi.org/10.1038/s41467-024-48809-w

Yu, G., Upadhyaya, P., Fan, Y., Alzate, J. G., Jiang, W., Wong, K. L., Takei, S., Bender, S. A., Chang, L.-T., Jiang, Y., Lang, M., Tang, J., Wang, Y., Tserkovnyak, Y., Amiri, P. K., & Wang, K. L. (2014). Switching of perpendicular magnetization by spin–orbit torques in the absence of external magnetic fields. Nature Nanotechnology, 9(7), 548–554. https://doi.org/10.1038/nnano.2014.94

Ziebel, M. E., Feuer, M. L., Cox, J., Zhu, X., Dean, C. R., & Roy, X. (2024). CrSBr: An Air-Stable, Two-Dimensional Magnetic Semiconductor. Nano Letters, 24(15), 4319–4329. https://doi.org/10.1021/acs.nanolett.4